MUSE searches for galaxies near very metal-poor gas clouds at $z \sim 3$: new constraints for cold accretion models

Michele Fumagalli,[1][*] Sebastiano Cantalupo,[2] Avishai Dekel,[3] Simon L. Morris,[1] John M. O'Meara,[4] J. Xavier Prochaska[5,6] and Tom Theuns[1]

[1]*Institute for Computational Cosmology and Centre for Extragalactic Astronomy, Department of Physics, Durham University, South Road, Durham DH1 3LE, UK*
[2]*Institute for Astronomy, ETH Zurich, Wolfgang-Pauli-Strasse 27, CH-8093 Zurich, Switzerland*
[3]*Racah Institute of Physics, The Hebrew University, Jerusalem 91904, Israel*
[4]*Department of Chemistry and Physics, Saint Michael's College, One Winooski Park, Colchester, VT 05439, USA*
[5]*Department of Astronomy and Astrophysics, University of California, 1156 High Street, Santa Cruz, CA 95064, USA*
[6]*University of California Observatories, Lick Observatory 1156 High Street, Santa Cruz, CA 95064 USA*

ABSTRACT

We report on the search for galaxies in the proximity of two very metal-poor gas clouds at $z \sim 3$ towards the quasar Q0956+122. With a 5-hour Multi-Unit Spectroscopic Explorer (MUSE) integration in a $\sim 500 \times 500$ kpc^2 region centred at the quasar position, we achieve a ≥ 80 per cent complete spectroscopic survey of continuum-detected galaxies with $m_R \leq 25$ mag and Lyα emitters with luminosity $L_{\mathrm{Ly}\alpha} \geq 3 \times 10^{41}$ erg s^{-1}. We do not identify galaxies at the redshift of a $z \sim 3.2$ Lyman limit system (LLS) with $\log Z/Z_{\odot} = -3.35 \pm 0.05$, placing this gas cloud in the intergalactic medium or circumgalactic medium of a galaxy below our sensitivity limits. Conversely, we detect five Lyα emitters at the redshift of a pristine $z \sim 3.1$ LLS with $\log Z/Z_{\odot} \leq -3.8$, while ~ 0.4 sources were expected given the $z \sim 3$ Lyα luminosity function. Both this high detection rate and the fact that at least three emitters appear aligned in projection with the LLS suggest that this pristine cloud is tracing a gas filament that is feeding one or multiple galaxies. Our observations uncover two different environments for metal-poor LLSs, implying a complex link between these absorbers and galaxy haloes, which ongoing MUSE surveys will soon explore in detail. Moreover, in agreement with recent MUSE observations, we detected a ~ 90 kpc Lyα nebula at the quasar redshift and three Lyα emitters reminiscent of a 'dark galaxy' population.

Key words: galaxies: formation – galaxies: haloes – galaxies: high-redshift – intergalactic medium – quasars: absorption lines – quasars: individual: Q0956+122.

1 INTRODUCTION

The assembly and growth of galaxies throughout cosmic times requires the continuous accretion of substantial amounts of fresh fuel. Observations of molecular or atomic gas in the interstellar medium of both high-redshift systems and nearby galaxies reveal that without accretion rates that are at least commensurable with the observed star formation rates (SFRs), galaxies would exhaust their gas reservoirs on time-scales of ~ 1–2 Gyr, much shorter than the Hubble time (e.g. Sancisi et al. 2008; Genzel et al. 2010). From this consideration, it follows that the accretion of gas from the halo (i.e. the circumgalactic medium or CGM) and, ultimately, from the baryon reservoir present in the intergalactic medium (IGM) needs to be ubiquitous at all redshifts.

In support of this argument, modern cosmological simulations predict accretion rates of $\gtrsim 10$–20 M$_{\odot}$ yr^{-1} at $z \sim 2$–3 galaxies (e.g. Dekel et al. 2009; Kereš et al. 2009; Faucher-Giguère, Kereš & Ma 2011). However, despite a general consensus that gas accretion is a dominant process for galaxy evolution, direct observational evidence of cold gas infalling on to galaxies is scarce at $z \sim 1$ (Martin et al. 2012; Rubin et al. 2012) and even more tenuous at higher redshifts (e.g. Bouché et al. 2013; Crighton et al. 2013; Martin et al. 2015). While in apparent contradiction with expectations of ubiquitous inflows, the lack of direct detections is often justified in the context of the so-called 'cold stream' or 'cold flow' paradigm if a significant fraction of the gas is accreted along narrow and dense filaments of cold gas (e.g. Birnboim & Dekel 2003; Kereš et al. 2005; Dekel & Birnboim 2006). Indeed, if the infalling gas covers

[*] E-mail: michele.fumagalli@durham.ac.uk

Table 1. Physical properties of the two LLSs, which are measured in absorption or inferred via photoionization modelling.

ID	z_{abs}	$\log N_{HI}$ (cm^{-2})	$\log Z/Z_\odot$	$\log n_H$ (cm^{-3})	$\log x_{HI}$	$\log \ell$ (pc)
LLS 1	3.096221 ± 0.000009	17.18 ± 0.04	< -3.8	< -2.0	< -2.4	> 3.1
LLS 2	3.223194 ± 0.000002	17.36 ± 0.05	-3.35 ± 0.05	-3.3	-4.1	6.3

Notes. The columns of the table are: (1) the system ID; (2) the redshift measured in absorption; (3) the neutral hydrogen column density measured in absorption; (4) the inferred metallicity; (5) the inferred neutral fraction; (6) the inferred size. Values are from Fumagalli et al. (2011a) and Lehner et al. (2016).

only a small fraction of the solid angle as seen from a galaxy (e.g. Goerdt et al. 2012), then it is natural that only a limited number of sightlines will intersect these infalling cold streams, showing redshifted absorption lines. Moreover, for typical infall velocities of $\sim$100–200 km s^{-1}, the signature of inflows is often masked by interstellar absorption at the systemic redshifts (Rubin et al. 2012). Further, when selecting absorbers via metal lines, some ambiguity remains in separating recycled gas falling back on to galaxies from material that is being accreted from the IGM for the first time.

Due to these intrinsic limitations, observers have to resort to other, more indirect, signatures of the presence of cold gas accretion. For instance, simulations predict that accretion in the form of cold flows is a dominant contributor to the cross-section of optically thick gas ($N_{HI} \geq 10^{17.2}$ cm^{-2}) that gives rise to Lyman limit systems (LLSs) near galaxies (e.g. Faucher-Giguère & Kereš 2011; Fumagalli et al. 2011b; van de Voort et al. 2012). While cold streams occupy only a small fraction of the solid angle seen from a galaxy, the probability to intersect these filaments in the transverse direction with background sources is higher. Indeed, simulations predict covering factors f_c for optically thick gas within the virial radius in the range of $f_c \sim 0.1$–0.4, although with large variations between different models (Faucher-Giguère & Kereš 2011; Fumagalli et al. 2011b, 2014a; Shen et al. 2013; Faucher-Giguère et al. 2015). Thus, in principle, statistical comparisons between the observed properties of LLSs near galaxies (e.g. Rudie et al. 2012; Prochaska, Hennawi & Simcoe 2013) and the predictions of numerical simulations offer interesting constraints for the cold accretion paradigm (see also Lehner et al. 2013; Fumagalli et al. 2014a; Cooper et al. 2015; Fumagalli, O'Meara & Prochaska 2016).

On an object-by-object basis, however, the lack of direct kinematic signatures of infall requires that multiple diagnostics are combined to establish whether the gas observed in absorption is potentially being accreted on to galaxies observed in emission at close projected separations. A few examples that rely on low metallicity (e.g. Ribaudo et al. 2011; Crighton et al. 2013; Lehner et al. 2013), rotational signatures (e.g. Bouché et al. 2013; Martin et al. 2015), or filamentary morphology (e.g. Cantalupo, Lilly & Haehnelt 2012) can be found in the literature. Following this approach, we present in this paper a dedicated search of galaxies around two very metal-poor LLSs with $Z \lesssim 5 \times 10^{-4}$ $Z_\odot$. Their extremely low metallicity is at odds with that expected for gas that has been enriched by outflows. Thus, even without direct kinematic measurements, metal-poor LLSs that reside near galaxies are among the most compelling examples of nearly chemically pristine gas infalling for the first time inside haloes. It is, however, worth noting that very metal-poor LLSs represent only a small fraction of the parent population, with $\lesssim$20 per cent of the LLSs having $Z \lesssim 10^{-3}$ $Z_\odot$ between $z \sim 2.5$ and 3.5 (Fumagalli et al. 2016; Lehner et al. 2016).

Our observations target the field of the quasar Q0956+122 (a.k.a. SDSSJ095852.19+120245.0), which lies at a redshift $z_{qso} = 3.3088 \pm 0.0003$ (Hewett & Wild 2010) and hosts two strong absorption line systems along its line of sight (Fumagalli, O'Meara & Prochaska

2011a): a pristine gas cloud at $z_{lls,1} = 3.096221 \pm 0.000009$ with H I column density[1] $\log N_{HI} = 17.18 \pm 0.04$ and without discernible metals to a limit of $Z < 10^{-3.8}$ $Z_\odot$; and a second LLS at $z_{lls,2} = 3.223194 \pm 0.000002$, with column density $\log N_{HI} = 17.36 \pm 0.05$ and metallicity $\log Z/Z_\odot = -3.35 \pm 0.05$ (Lehner et al. 2016). A summary of the physical properties measured for these two systems or inferred via photoionization modelling by Fumagalli et al. (2011a) and Lehner et al. (2016) is presented in Table 1.

Details of the imaging and spectroscopic observations are presented in Section 2, followed by the analysis of continuum-detected sources and Lyα emitters in Sections 3 and 4. In Section 5, we report on the discovery of an extended nebula at the quasar redshift, with discussion and conclusions in Section 6. Given the technical nature of Sections 2–4, readers who are primarily interested in the final results may prefer to continue reading from Section 5. Throughout this work, we assume solar abundances from Asplund et al. (2009) with $Z_\odot = 0.0134$, and we use the 'Planck 2013' cosmology (Planck Collaboration XVI et al. 2014) for which the Hubble constant is $H_0 = (67.8 \pm 0.8)$ km s^{-1} Mpc^{-1} and the matter density parameter is $\Omega_m = 0.308 \pm 0.010$. Magnitudes are expressed in the AB system.

2 OBSERVATIONS AND DATA PROCESSING

2.1 Imaging observations

Imaging observations of the Q0956+122 field were obtained using LRIS (Oke et al. 1995) at Keck, as part of the NOAO programmes 2013A-0078 and 2013B-0102 (PI Fumagalli). Thanks to the dual-arm design of LRIS, we acquired with the D460 dichroic a 5400-s exposure using the u' filter on the blue side camera, together with a 1440-s exposure using the V filter, and two 1080-s exposures in the R and I filters on the red side camera. Observations were conducted on UT 2013 March 9 when the target was transiting at an airmass of $\sim$1.1 under variable conditions.

Imaging data have been processed and calibrated following the procedures described in Fumagalli et al. (2014b), including basic calibrations (bias and flat-fielding corrections), and photometric and astrometric calibrations. Due to poor seeing and patchy clouds, the resulting image quality is modest, with a point source full-width at half-maximum (FWHM) of 1.5 arcsec in u', 1.2 arcsec in V, 1.3 arcsec in R, and 1.3 arcsec in I. However, we recalibrate these images using the high-quality Sloan Digital Sky Survey (SDSS) photometry (Alam et al. 2015) for bright stars in the field, achieving errors on the flux calibration within $\sim$0.06–0.05 mag for all filters. This is confirmed by the excellent agreement between R-band magnitudes measured in LRIS images and images reconstructed from the Multi-Unit Spectroscopic Explorer (MUSE) data collected for most part in photometric conditions (see below).

---

[1] Throughout this work, H I column densities are expressed in units of cm^{-2}.

For each filter, we measure the noise properties and we extract source catalogues as described in Fumagalli et al. (2014b). For an aperture of 2 arcsec in diameter, we find a 2σ magnitude detection limit of 27.7 mag in u', 26.9 mag in V, 26.6 mag in R, and 26.3 mag in I.

2.2 Spectroscopic observations

High-resolution spectroscopy of the Q0956+122 quasar is available from the Keck HIRES archive, and the analysis of this spectrum has been presented in Fumagalli et al. (2011a) and Lehner et al. (2016).

In addition to high-resolution spectroscopy for the quasar, we have acquired integral field unit (IFU) spectroscopy within a square region of ~1.1 arcmin on a side centred at the quasar position. Observations have been conducted using the MUSE (Bacon et al. 2010) at the UT4 Very Large Telescope (VLT) as part of the programme 094.A-0280(A) in period 94 (PI Fumagalli). Data have been acquired in Wide Field Mode using slow guiding and the extended wavelength mode to ensure non-zero throughput down to 4650 Å. A total of 4.1 h on source was acquired in sets of 1500-s exposures. A dither pattern with ~5 arcsec steps and $90°$ rotation was adopted to map a 68×68 arcsec^2 region around Q0956+122 with the $\sim60 \times 60$ arcsec^2 MUSE field of view. With this pattern, we achieve maximum depth within the inner 40×40 arcsec^2, while in the outer region the sensitivity decreases radially from the quasar position. All observations were conducted in dark time, with seeing $\lesssim0.8$ arcsec, and at airmass <1.7 (with an average of ~1.3) in clear or photometric conditions.

Data have been reduced using a combination of recipes from the ESO MUSE pipeline (v1.2.1; Weilbacher et al. 2014) and the CUBEXTRACTOR package (CUBEX in short, version 1.5; Cantalupo, in preparation), supplemented by in-house Python codes. First, we create a master bias and a master flat with the MUSE pipeline, together with a wavelength solution and an illumination correction using twilight flats. Next, we apply these calibrations to the science exposures and the standard stars used for spectro-photometric flux calibrations. Data cubes for individual exposures are constructed using a common reference grid with voxels of 1.25 Å in the spectral direction and 0.2 arcsec in the spatial direction. At this stage, the pipeline applies a barycentric correction. Subsequently, using CubeFix and CubeSharp within the CUBEX package, we improve the quality of the flat-field correction, and perform a flux-conserving sky subtraction on individual cubes (for details see e.g. Borisova et al. 2016). The last two steps are then repeated using the cubes from the previous iteration to identify and mask sources in white-light images reconstructed from the cubes, and thus minimizing the contamination from sources when computing illumination corrections. In the end, all individual exposures are combined in a final cube using mean statistics. To help with source identification, we also construct a second cube using median statistics that better rejects residual cosmic rays and artefacts in individual exposures. The wavelength calibration of MUSE data is performed in air, but we apply appropriate transformation to vacuum when comparing to HIRES data and measuring redshifts.

Before proceeding with our analysis, we also perform a series of tests on the quality of the final MUSE data cube. The final depth (root mean square) of the data cube is 5×10^{-19} erg s^{-1} cm^{-2} Å^{-1} arcsec^{-2} as measured in a 10 Å window centred at 5000 Å in empty regions near the quasar position (4×10^{-19} erg s^{-1} cm^{-2} Å^{-1} arcsec^{-2} at 6000 Å). Next, we test for the absolute flux calibration by comparing the R-band magnitudes of sources detected in a MUSE reconstructed image against values from our deep Keck imaging, finding a difference of <0.05 mag in agreement with calibration errors. At this stage, we also verify the final image quality of the MUSE cubes, finding a mean FWHM of 0.67 ± 0.02 arcsec for point sources. We also examine the relative flux calibration and the wavelength solution by comparing the MUSE and SDSS spectrum for the central quasar, again finding excellent agreement.

3 PROPERTIES OF CONTINUUM DETECTED SOURCES

3.1 Source extraction and aperture photometry

Using the MUSE median data cube, we produce a deep detection image by collapsing the cube along the wavelength axis. We then construct a source catalogue from the detection image by running SEXTRACTOR (Bertin & Arnouts 1996) with a detection area of 8 pixels and a threshold of $1.5\sigma_{rms}$, where σ_{rms} is the background root mean square. Only sources within a box of 65 arcsec on the side (~500 kpc at the redshift of the two LLSs) and centred at the quasar position are considered in the following analysis, in order to avoid spurious detections arising from edge effects and to prevent the inclusion of sources with partial coverage.

Next, using the segmentation map, we extract 1D spectra for each source from both the mean and median cubes, together with a 2D spectrum obtained by collapsing the data cube along one spatial axis. At this stage, wavelengths are shifted to vacuum for consistent redshift determinations in both HIRES and MUSE data. A list of the 91 extracted sources, detailing the positions and magnitudes of each object, is provided in Table 2. Sources are also identified within the MUSE field of view in Fig. 1.

Throughout this work, we report magnitudes computed inside the Kron radius (Kron 1980), as derived from the deep detection image. The same apertures, with appropriate astrometric transformations, are also used to extract the photometry from the Keck images. To account for the different image quality between the MUSE and Keck data, we apply a wavelength-dependent aperture correction that is computed by taking the ratio of the seeing measurements in the Keck broad-band images and the MUSE data cube. Agreement is found when comparing magnitudes extracted from the LRIS R-band image and an equivalent R-band image reconstructed from the MUSE data cube, providing a consistency check on both our procedures and calibrations. We emphasize, however, that while colours computed within the MUSE data cube are very robust, colours computed across instruments are more sensitive to residual offsets in the astrometric calibrations. Errors on the LRIS magnitudes are derived from the noise image following Fumagalli et al. (2014b), while errors on MUSE magnitudes are computed directly from the variance cube. These errors are used to compute upper limits for non-detections, hereafter quoted at 2σ confidence level.

With R-band magnitudes for all the detected sources, we derive a simple metric of completeness by observing that the galaxy counts reach a peak around $m_R \sim 26$ mag, and steeply fall off at fainter magnitudes.

3.2 Spectroscopic redshifts

To measure the redshift of the continuum detected sources, we first visually inspect each spectrum in 1D and 2D to search for emission and absorption lines. Weak features are confirmed by inspecting spectra from the mean and median cubes. When multiple

Table 2. Properties of the sources with continuum detection.

ID	R.A. (deg)	Dec. (deg)	m_R (mag)	$m_{u'}$ (mag)	D_{qso} (arcsec)	z_{spec}	Notes
1	149.72597	12.03741	23.91 ± 0.12	25.02 ± 0.19	42.6	0.6502	
2	149.72082	12.03758	26.13 ± 0.40	>26.11	32.0	–	
3	149.72184	12.03755	25.80 ± 0.30	>26.65	33.6	–	
4	149.71657	12.03795	26.82 ± 0.51	>26.64	28.6	–	
5	149.72446	12.03765	23.02 ± 0.09	23.75 ± 0.12	38.4	0.9456	
6	149.71433	12.03789	24.60 ± 0.19	25.26 ± 0.25	30.6	0.8436	
7	149.71970	12.03836	27.33 ± 0.69	>26.65	28.0	–	
8	149.70935	12.03815	24.70 ± 0.21	24.84 ± 0.28	39.7	1.0306	
9	149.71694	12.03852	25.53 ± 0.26	>26.65	26.4	–	
10	149.71042	12.03869	26.11 ± 0.35	>26.65	35.7	–	
11	149.71261	12.03869	22.63 ± 0.07	23.42 ± 0.03	30.9	0.8177	
12	149.71797	12.03901	26.07 ± 0.34	>26.65	24.6	1.2193*	Sky residuals
13	149.70999	12.03913	26.38 ± 0.40	>26.65	35.7	–	
14	149.71043	12.03948	26.52 ± 0.44	>26.65	33.7	–	
15	149.71582	12.03973	26.82 ± 0.51	>26.65	22.7	–	
16	149.72151	12.03988	25.69 ± 0.28	27.30 ± 0.71	25.7	–	
17	149.71362	12.04007	26.29 ± 0.38	>26.65	24.8	–	
18	149.71180	12.03994	24.88 ± 0.19	>26.64	29.1	0.3391	
19	149.72510	12.04049	26.44 ± 0.39	>26.65	33.1	–	
20	149.72223	12.04033	24.63 ± 0.17	25.77 ± 0.22	26.0	0.2555*	[O III]+Mg I?
21	149.71564	12.04053	25.79 ± 0.30	>26.65	20.1	0.5084	
22	149.71723	12.04069	24.45 ± 0.16	>26.65	18.5	0.8518	
23	149.71102	12.04081	25.78 ± 0.31	26.62 ± 0.45	29.0	1.0565	
24	149.72658	12.04083	24.00 ± 0.13	25.43 ± 0.47	36.8	1.0058*	Sky residuals
25	149.71526	12.04143	27.06 ± 0.59	>26.65	17.6	–	
26	149.72228	12.04146	25.58 ± 0.27	26.15 ± 0.30	23.1	0.0485	
27	149.72179	12.04156	23.60 ± 0.11	26.05 ± 0.28	21.7	0.8516	
28	149.71056	12.04246	26.54 ± 0.48	26.38 ± 0.36	27.2	–	
29	149.72560	12.04250	26.49 ± 0.43	>26.65	31.1	–	
30	149.71110	12.04253	26.68 ± 0.49	27.30 ± 0.71	25.4	–	
31	149.72624	12.04309	25.23 ± 0.23	25.67 ± 0.27	32.5	–	
32	149.72210	12.04305	25.73 ± 0.29	26.73 ± 0.47	19.2	–	
33	149.71597	12.04290	22.46 ± 0.06	26.46 ± 0.38	11.8	0.0000	Star
34	149.71990	12.04321	25.09 ± 0.22	26.98 ± 0.57	12.8	0.0439*	Hα?
35	149.72512	12.04320	23.69 ± 0.11	24.14 ± 0.05	28.6	1.0847	
36	149.71273	12.04354	26.08 ± 0.35	>26.65	18.6	–	
37	149.71955	12.04381	27.24 ± 0.63	25.91 ± 0.25	10.4	–	
38	149.71921	12.04394	25.99 ± 0.33	27.39 ± 0.75	9.2	1.2003	
39	149.71612	12.04377	23.46 ± 0.10	23.72 ± 0.04	8.8	1.0091	
40	149.71563	12.04386	23.69 ± 0.11	23.61 ± 0.03	9.6	1.0090	
41	149.72536	12.04408	26.54 ± 0.44	26.49 ± 0.39	28.5	–	
42	149.72179	12.04396	23.83 ± 0.12	25.38 ± 0.16	16.7	0.8520	
43	149.72396	12.04424	25.83 ± 0.31	>26.65	23.6	1.1315	
44	149.71410	12.04436	26.41 ± 0.40	>26.64	13.0	–	
45	149.72508	12.04439	27.15 ± 0.62	>26.65	27.3	–	
46	149.71486	12.04449	26.94 ± 0.53	>26.65	10.4	–	
47	149.72305	12.04453	25.85 ± 0.31	26.78 ± 0.48	20.2	1.0862*	Sky residuals
48	149.72116	12.04515	26.31 ± 0.36	>26.65	13.3	–	
49	149.72133	12.04538	26.88 ± 0.46	>26.65	13.7	1.1574	
50	149.72225	12.04547	26.32 ± 0.36	>26.66	16.9	–	
51	149.72594	12.04565	25.14 ± 0.22	25.82 ± 0.23	29.9	0.8051	
52	149.71097	12.04589	25.39 ± 0.25	>26.65	22.8	–	
53	149.72528	12.04600	26.74 ± 0.48	>26.65	27.6	–	
54	149.70978	12.04600	25.34 ± 0.24	>26.65	27.1	4.0520	
55	149.70866	12.04616	26.17 ± 0.36	26.43 ± 0.37	31.0	–	
56	149.71967	12.04626	26.18 ± 0.35	>26.65	7.9	0.8506	
57	149.71527	12.04683	26.89 ± 0.51	>26.65	8.5	–	
58	149.72025	12.04700	26.21 ± 0.36	>26.65	10.7	–	
59	149.71749	12.04586	17.16 ± 0.01	20.74 ± 0.00	0.0	3.3088	Quasar
60	149.71211	12.04761	26.90 ± 0.59	>26.43	19.9	–	
61	149.72636	12.04753	25.08 ± 0.20	26.90 ± 0.55	31.9	0.2668	
62	149.72430	12.04779	26.40 ± 0.43	>26.65	25.1	–	
63	149.72117	12.04747	23.10 ± 0.09	24.43 ± 0.07	14.3	0.3752	
64	149.71294	12.04782	26.87 ± 0.53	>26.65	17.4	–	

Table 2 – *continued*

ID	R.A. (deg)	Dec. (deg)	m_R (mag)	$m_{u'}$ (mag)	D_{qso} (arcsec)	z_{spec}	Notes
65	149.71665	12.04836	27.58 ± 0.65	>26.65	9.5	1.5572	
66	149.72590	12.04835	22.92 ± 0.08	24.15 ± 0.07	31.1	0.5491	
67	149.72020	12.04903	24.23 ± 0.14	>26.65	15.0	0.3554	
68	149.72511	12.04942	26.92 ± 0.56	>26.65	29.9	–	
69	149.70876	12.04899	21.70 ± 0.05	24.16 ± 0.18	32.7	0.2710	
70	149.71668	12.04971	25.12 ± 0.21	27.19 ± 0.65	14.2	–	
71	149.72502	12.05005	>26.78	>26.65	30.7	–	
72	149.71128	12.05010	26.29 ± 0.38	>26.65	26.6	–	
73	149.71996	12.05011	25.74 ± 0.29	>26.65	17.7	0.3336	
74	149.72332	12.04997	23.02 ± 0.08	24.46 ± 0.10	25.5	0.5556	
75	149.71829	12.05040	25.86 ± 0.29	>26.65	16.7	0.0740*	Hα?
76	149.72576	12.05124	>27.39	>26.65	35.1	–	
77	149.72631	12.05122	23.88 ± 0.12	26.01 ± 0.29	36.7	0.3555*	Template match
78	149.71276	12.05154	26.78 ± 0.52	>26.65	26.4	–	
79	149.71809	12.05108	23.88 ± 0.12	24.78 ± 0.13	19.0	2.1311	
80	149.71807	12.05165	23.47 ± 0.10	24.99 ± 0.13	21.0	0.5850	
81	149.71660	12.05191	26.65 ± 0.43	>26.65	22.1	–	
82	149.72401	12.05187	25.94 ± 0.33	26.65 ± 0.44	31.7	1.2034	
83	149.71566	12.05193	25.22 ± 0.23	25.30 ± 0.15	22.8	2.2912	
84	149.71360	12.05194	24.64 ± 0.17	25.14 ± 0.13	25.8	0.5094	
85	149.71313	12.05217	24.98 ± 0.22	24.72 ± 0.12	27.4	0.8691*	Mg II?
86	149.71525	12.05235	25.36 ± 0.25	>26.64	24.7	–	
87	149.71621	12.05310	26.65 ± 0.45	>26.65	26.5	–	
88	149.71673	12.05323	27.09 ± 0.60	27.26 ± 0.68	26.8	0.1401*	Hα?
89	149.71614	12.05382	26.00 ± 0.33	>26.65	29.1	4.1196*	Lyα?
90	149.71905	12.05287	22.77 ± 0.08	23.34 ± 0.08	26.0	0.6230	
91	149.71914	12.05383	21.10 ± 0.04	22.88 ± 0.05	29.4	0.5562	

Notes. The columns of the table are: (1) the source ID; (2,3) the source position (J2000); (4) the R-band magnitude from MUSE data; (5) the u'-band magnitude from LRIS data; (6) the distance from the quasar; (7) the spectroscopic redshift. For non-detections, we quote 2σ limits. Here we report observed magnitudes not corrected for galactic extinction. Asterisks mark uncertain redshift determinations due to single emission/absorption lines, or identification of absorption lines in low S/N spectra or next to sky lines.

absorption and emission lines are identified, we determine redshifts from Gaussian fits to the emission lines, with typical errors of $\delta z \sim 0.0002$–0.0003. For sources without emission lines, instead, we compare spectra to templates from SDSS/DR5 (Adelman-McCarthy et al. 2007) or to Lyman Break Galaxy (LBG) templates from Bielby et al. (2013) using a custom-made graphical user interface. For the few cases in which a single emission or absorption line is detected and no other strong unambiguous features are visible, we assign a tentative redshift as described in Table 2. Following these steps, we measure redshifts for 48/91 sources (38/91 with robust redshifts), achieving a nearly complete spectroscopic redshift survey for sources with $m_R \leq 25$ mag (with 24/28 sources having robust redshifts). A summary of redshift measurements is provided in Table 2, which reveals no association with the two LLSs.

In passing, we note the presence of a group of at least four sources at $z \sim 0.85$ (ID 22, 27, 42, 56) which is within $\sim 300\,\mathrm{km\,s^{-1}}$ from a Mg II absorption system detected at $z = 0.85010 \pm 0.00001$. Among these sources, ID 56 lies at a projected separation of ~ 8 arcsec or $\sim 60\,\mathrm{kpc}$ from the absorption line system, at nearly coincident redshift.

3.3 Colour selection of $z \sim 3.0$–3.3 galaxies

For galaxies with $m_R > 25$ mag for which our spectroscopic redshift survey becomes severely incomplete, we investigate with colour information whether the MUSE field of view contains galaxies with spectral energy distributions (SEDs) consistent with sources at $z \sim 3.0$–3.3. To this end, we generate observed SEDs for all the sources with continuum detection in the MUSE data cube using six photometric data points, which are extracted from the Keck u'-band image and from five medium-band images from the MUSE data cube with a 500 Å wide top-hat filter centred at 4900 Å, 5400 Å, 5900 Å, 6400 Å, and 6900 Å. At this stage, we also correct the observed magnitudes for the wavelength-dependent Galactic extinction, following Schlafly & Finkbeiner (2011). For the broad-band photometry reported in Table 2, these corrections are $A_{u'} = 0.15$ mag and $A_R = 0.07$ mag.

To search for sources with colours consistent with $z \sim 3.0$–3.3 galaxies, we use the EAZY code (Brammer, van Dokkum & Coppi 2008). Using sources with a spectroscopic redshift as a test bed (at redshifts $z < 3$), we find that our photometry does not span a sufficient wavelength range to remove the well-known degeneracy between low- and high-redshift sources. Moreover, and perhaps most importantly, the u'-band image was acquired in modest weather conditions, thus limiting the constraining power of the (weak) upper limits from the LRIS u'-band image. This fact is indeed reflected by the broad redshift range spanned by the likelihood functions. For this reason, when integrating the redshift probability distribution function derived assuming a flat prior on the magnitude in the redshift interval $z = [3.0, 3.3]$, we do not identify any galaxy with a significant probability excess ($\gtrsim 50$ per cent) in the interval of interest. Only three sources (ID 52, 53, and 86) exhibit a modest excess of ~ 25–30 per cent, but the broad shape of the posterior redshift distribution function prevents us from conclusively identifying any of them as the host of one of the two LLSs.
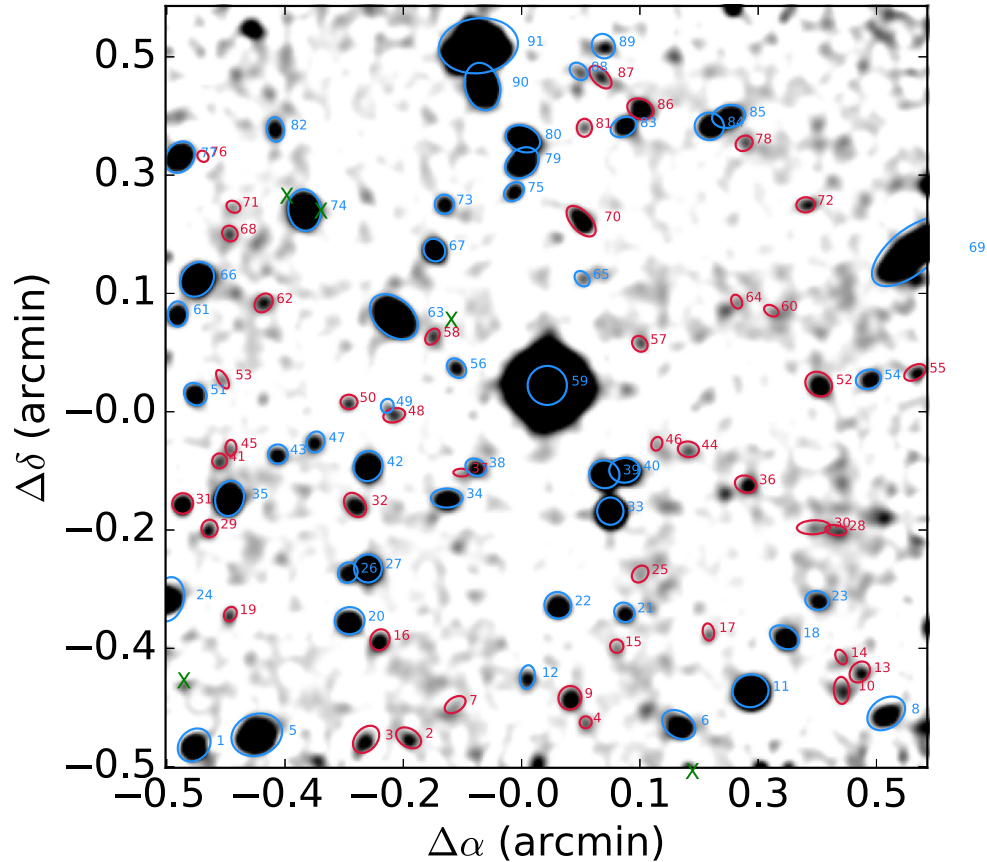
Figure 1. Image of the square region (~1.1 arcmin on a side) centred at the position of Q0956+122, from a deep white-light image reconstructed by collapsing the MUSE data cube along the wavelength axis. The position of each continuum-detected source is marked with an aperture and the source ID. In blue, we identify sources for which a spectroscopic redshift has been measured, while in red we mark sources without spectroscopic redshifts. Green crosses mark Lyα emitters (see also Fig. 5). Some sources are visible at the edge of the field, but they are not included in our analysis due to partial coverage or lower data quality in the periphery of the field of view.

4 PROPERTIES OF LINE EMITTERS

We focus next on the detection and characterization of line emitters which, due to their faint continuum level, may be undetected in the deep white-light image. Throughout this section, we make use of the CUBEX capability (Cantalupo, in preparation) of identifying sources in three dimensions by searching for groups of contiguous voxels in the MUSE data cube above a desired signal-to-noise ratio (S/N) threshold both in the spatial direction and along the wavelength axis.

We search for line emitters in proximity of the two intervening LLSs within a window of about $\pm 1000\,\mathrm{km\,s^{-1}}$, running CUBEX on the mean cube,[2] after having subtracted the quasar point spread function (PSF) and the continuum emission of each source as described in Borisova et al. (2016). To ensure the highest completeness to faint fluxes, we extract candidate sources with a minimum volume of 50 voxels at S/N $\geq$ 3. At this step, the cube is convolved in the spatial direction with a boxcar filter of 2 pixels and the variance cube is rescaled by a factor of ~1.8 (weakly dependent on wavelength) to match the value measured within the data cube.

After having identified the sources, we visually inspect optimally extracted line flux images (for details, see Borisova et al. 2016) from

both the mean and median cube. To avoid the inclusion of spurious sources (e.g. cosmic rays residuals or image defects arising from the edges of the frame), we also construct line flux images from two independent cubes containing only one of the two exposures collected in each observing block. Following visual inspection, a source is included in the final catalogue if it is detected both in the mean and median cubes, as well as in the two independent cubes constructed from half of all the exposures available. While this choice affects the recovery fraction at the faint end of the flux distribution, it ensures that only reliable sources are included in the final analysis.

Finally, we extract 1D spectra and measure redshifts by fitting Gaussian functions to the emission lines. Sources are classified as Lyα emitters if the emission line is not resolved, which would be indicative of [OII] emission, and no positive identification of other emission lines (Hα, [OIII], Hβ) is made in the spectrum.

In a window of about $\pm 1000\,\mathrm{km\,s^{-1}}$ centred at redshift of the $z \sim 3.1$ LLS, we identify six line emitters, five of which are classified as Lyα sources. The remaining source is an [OII] emission line coinciding with the continuum-detected galaxy ID 18. Conversely, at the redshift of $z \sim 3.2$ LLS, we detect only one source with more than 50 voxels above S/N = 3, which is a strong, spatially resolved, [OII] emission line associated with the galaxy ID 63 at $z \sim 0.3752$. No other sources are identified as Lyα emitters within this region of the cube.

---

[2] We defer the search of emitters across the entire cube to future work within our ongoing Large Programme (197.A-0384).

Table 3. Properties of the Lyα emitters near to the pristine $z \sim 3.1$ LLS.

ID	R.A. (deg)	Dec. (deg)	Δv (km s^{-1})	D_{qso} (kpc,″)	$F_{Ly\alpha}(10^{-18}$ erg s^{-1} cm^{-2})
1–3	149.72298	12.04986	−1149	189.5, 24.26	5.9 ± 0.5
1–12	149.72627	12.03883	−375	312.4, 40.00	13.7 ± 1.1
1–21	149.71985	12.04730	795	77.7, 9.95	4.0 ± 0.4
1–25	149.72380	12.05021	861	213.4, 27.32	3.4 ± 0.4
1–26	149.71406	12.03670	1033	273.4, 35.01	3.6 ± 0.6

Notes. The columns of the table are: (1) the source ID; (2,3) the source position; (4) the relative velocity along the line of sight with respect to the LLS, with typical errors of ∼15–20 km s^{-1}; (5) the projected distance relative to the quasar centroid where H I absorption is measured, with typical errors of ∼0.5 kpc or ∼0.06 arcsec; (6) the line flux integrated within the CuBEx segmentation map.
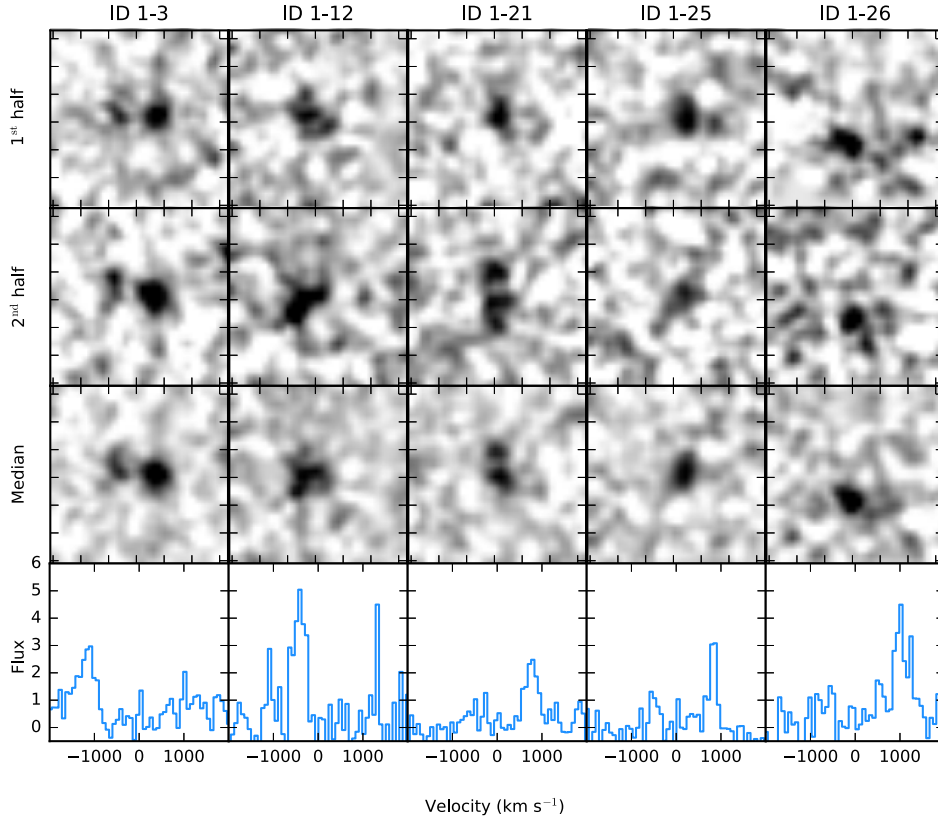
Figure 2. Gallery of the five Lyα emitters identified in proximity of the $z \sim 3.1$ LLS. Each emitter is shown in a column, where from top to bottom we show optimally extracted images obtained with CuBEx (Cantalupo, in preparation; see also Borisova et al. 2016) from two independent cubes each containing half of all the exposures and from the median cube. The bottom row shows the 1D spectra, with velocities relative to the LLS redshift and fluxes in units of 10^{-20} erg s^{-1} cm^{-2} Å^{-1}.

For each Lyα emitter detected near the $z \sim 3.1$ LLS, we also measure the distance from the quasar centroid where H I absorption is detected, and we integrate the line flux within the three-dimensional segmentation maps provided by CuBEx. While this choice maximizes the S/N of this measurement, fluxes should be regarded as formal lower limits, although we note modest differences when integrating the flux in a cubic region that encompasses the full extent of the detected emission line (see also below). A summary of the properties of the five Lyα emitters identified at the redshift of the $z \sim 3.1$ LLS is provided in Table 3 and Fig. 2.

Finally, we assess the completeness of our search for Lyα emitters by means of mock tests. Specifically, we populate the mean data cube (preserving the original noise) with line emitters with fluxes in the range $(2–7) \times 10^{-18}$ erg s^{-1} cm^{-2} and size defined by a two-dimensional Gaussian with 0.7 arcsec FWHM in the

spatial direction, and a Gaussian of 2.5 Å FWHM in the spectral direction. During this test, we inject 500 sources at the redshift of each LLS, which represents a compromise between reducing counting errors and avoiding blending of sources. We then process these mock cubes following the same analysis adopted for the real data, finding similar results for each LLS. The fraction of recovered sources combined for both LLSs is shown in Fig. 3, which indicates that our search is ≥80 per cent complete for line fluxes ≥3.5×10^{-18} erg s^{-1} cm^{-2}. As visible in the figure, occasional blending slightly reduces the completeness also at the bright end. At this stage, we also test the quality of the recovered line fluxes, finding that the discrepancy between the input and recovered fluxes is distributed as a Gaussian, the centre of which is consistent with zero to within the 1σ flux errors.
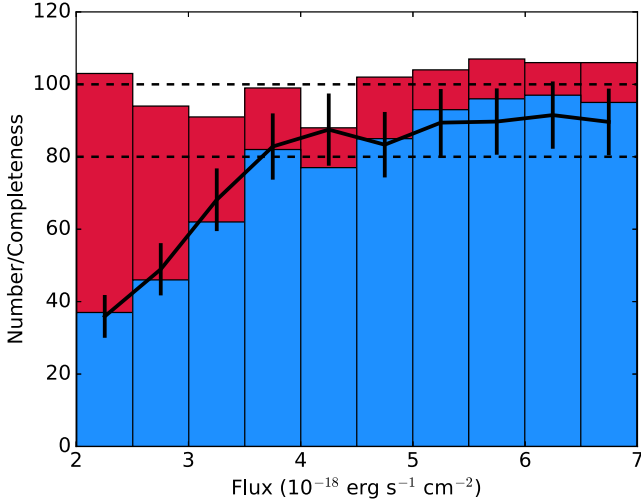
Figure 3. Results of a completeness test for the recovery of Lyα emitters between $z \sim 3.1$ and 3.2. In red, we show the input mock flux distribution, and in blue we show the number of sources identified by CUBEX. The black solid line shows the recovered fraction, including counting errors. Our search for Lyα emitters is ≥ 80 per cent complete for fluxes $\geq 3.5 \times 10^{-18} \, \mathrm{erg \, s^{-1} \, cm^{-2}}$.

5 AN EXTENDED NEBULA ASSOCIATED WITH THE QUASAR

Upon inspection of the data cube at wavelengths corresponding to Lyα at the redshift of the quasar, we identify extended diffuse emission as well as the presence of three compact emitters. After subtracting the quasar PSF and all continuum detected sources, we obtain a segmentation map for the diffuse emission by identifying with CUBEX pixels with S/N ≥ 2 inside a region of minimum area of 2000 voxels, chosen to be large enough to filter compact sources. To characterize the three emitters, we further run CUBEX to search for sources composed of at least 60 voxels with S/N ≥ 5. Fig. 4

shows the surface brightness map and 1D spectra of both the nebula and these Lyα emitters.

As shown in the figure, this nebula is highly asymmetric and extends in the east direction for up to ~ 12 arcsec, or $\sim 90 \, \mathrm{kpc}$ at the redshift of the quasar, with a surface brightness of $\geq 10^{-18} \, \mathrm{erg \, s^{-1} \, cm^{-2} \, arcsec^{-2}}$. While not as dramatic as some of the giant nebulae uncovered around $z \sim 2$ quasars (Cantalupo et al. 2014; Hennawi et al. 2015), this nebula is brighter than the typical nebulae seen around $z \sim 2$ quasars (Arrigoni Battaia et al. 2016), and it is comparable to the nebulae seen by MUSE at $z \sim 3$ around all bright radio-quiet quasars observed so far (e.g. Borisova et al. 2016). Kinematically, the bulk of the Lyα emission is redshifted by $\sim 500 \, \mathrm{km \, s^{-1}}$ when considering the quasar redshift measured from rest-frame UV lines (Fig. 4, top-right panel) and spans $\gtrsim 600 \, \mathrm{km \, s^{-1}}$ in velocity, with a second component extending to negative velocity.

The spectra of the three compact sources show prominent Lyα emission aligned in velocity space with the nebula (Fig. 4, bottom-right panel). No obvious signatures of a strong AGN component are evident from the spectra of these compact sources. The emitters have a line flux integrated over the segmentation map of $(8.4 \pm 0.4) \times 10^{-18} \, \mathrm{erg \, s^{-1} \, cm^{-2}}$ (source A), $(5.1 \pm 0.4) \times 10^{-18} \, \mathrm{erg \, s^{-1} \, cm^{-2}}$ (source B), and $(8.9 \pm 0.5) \times 10^{-18} \, \mathrm{erg \, s^{-1} \, cm^{-2}}$ (source C). As previously discussed, these values represent formally lower limits, as additional flux may be present outside of the voxels selected by the segmentation map. However, we have shown that this effect is expected to be a minor one, with all the flux being recovered typically within errors. Source A is also detected in the continuum, with an R-band magnitude of $m_R = 27.5 \pm 0.2$ mag computed inside an aperture matched to the size of the Lyα emission. However, we cannot exclude contamination from the nearby source ID 67 in close proximity to emitter A, and we consider this measurement an upper limit to the actual continuum. Conversely, source B and C are not detected in the continuum within the R-band image, to a limiting magnitude of 28.6 mag and 28.9 mag (2σ) within an aperture matched to the Lyα emission.
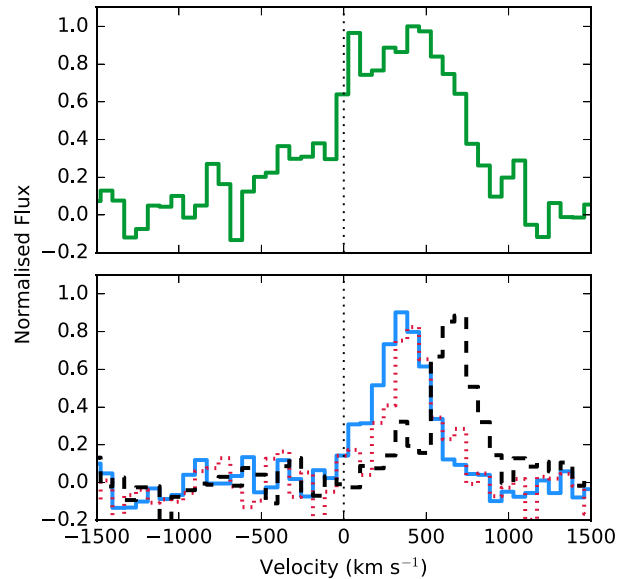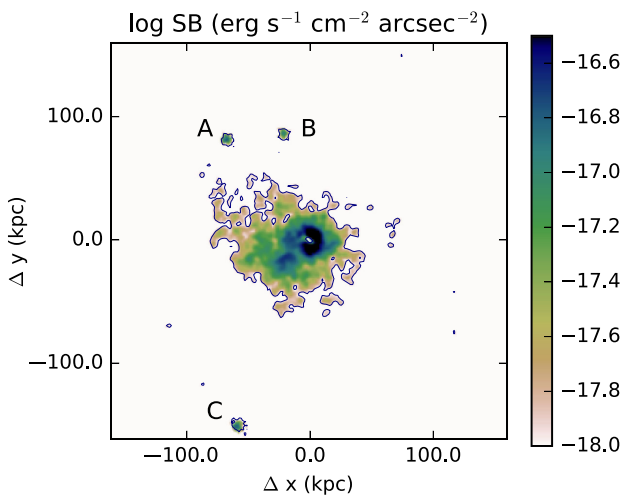

Figure 4. Left: Lyα surface brightness map of an extended nebula and of three Lyα emitters discovered at the quasar redshift. The image shows the surface brightness derived from optimally extracted line maps. The blue contour shows the $10^{-18} \, \mathrm{erg \, s^{-1} \, cm^{-2} \, arcsec^{-2}}$ level. Right: spectra integrated over the segmentation map for the extended nebula (top) and the three emitters (bottom; solid blue line for source A, red dotted line for source B, and black dashed line for source C). The velocity scale is centred at the quasar redshift derived from rest-frame UV lines (vertical dotted line).

With a luminosity of $L_{\text{Ly}\alpha} \geq 5 \times 10^{41}$ erg s^{-1} and lacking appreciable continuum emission, these sources are characterized by equivalent widths >100–140 Å in aperture matched to the extent of the Lyα emission, or >150–280 Å when adopting apertures matched to the seeing of the continuum image. Thus, these sources are reminiscent of the population of bright emitters, including 'dark galaxies' with equivalent widths in excess of 240 Å, reported by Cantalupo et al. (2012) around a bright quasar that boosts the Lyα emission intrinsic to the sources. Indeed, in a volume of ~ 150 Mpc^3 defined by the MUSE field of view and a velocity window of ± 1500 km s^{-1} around the quasar redshift, one would expect to see approximately two emitters according to the luminosity function presented in Cantalupo et al. (2012) when including the boost due to quasar radiation. This estimate is in line with our observations and a factor of ~ 5 above the expectation from the field luminosity functions (e.g. Cassata et al. 2011).

6 DISCUSSION AND CONCLUSIONS

Our analysis of a deep MUSE exposure in the field of the quasar Q0956+122 that hosts two very metal-poor LLSs provides a proof-of-concept of the power of IFU spectroscopy at large telescopes for addressing open questions on the nature of LLSs and their link with the CGM of galaxies as predicted by simulations (e.g. Faucher-Giguère & Kereš 2011; Fumagalli et al. 2011b, 2014a; Shen et al. 2013; Faucher-Giguère et al. 2015). Indeed, with a 5-h observation, we have achieved a ≥ 80 per cent complete spectroscopic survey for continuum-detected galaxies with $m_R \leq 25$ mag and for Lyα emitters with luminosity $L_{\text{Ly}\alpha} \geq 3 \times 10^{41}$ erg s^{-1}. This drastically improves on what was previously possible with narrow-band or (multi-object) spectroscopic surveys (e.g. Fynbo, Thomsen & Møller 2000; Rauch et al. 2008; Crighton et al. 2015).

In our observations, we do not identify bright continuum-detected sources at the redshift of the two LLSs, thus excluding a rapidly star-forming galaxy (i.e. a 'classic' LBG) with mean halo mass $\log M/M_\odot \sim 11.5$ (Bielby et al. 2013) and observed SFRs of $\gtrsim 6 \, M_\odot \, \text{yr}^{-1}$ as the host of these gas clouds. These are the galaxies that are generally targeted in studies of galaxy–quasar pairs (e.g. Rudie et al. 2012; Prochaska et al. 2013).

Furthermore, when searching for Lyα emitters near the metal-poor ($\log Z/Z_\odot = -3.35 \pm 0.05$) LLS at $z \sim 3.2$, we do not detect any source to a limiting luminosity of $L_{\text{Ly}\alpha} \geq 3 \times 10^{41}$ erg s^{-1} (uncorrected for dust or IGM absorption), corresponding to SFRs of $\gtrsim 0.2 \, M_\odot \, \text{yr}^{-1}$ (see Rauch et al. 2008) and for which our search is ≥ 80 per cent complete. The lack of any detection of Lyα emitters within a comoving volume of ~ 95 Mpc^{-3} defined by the MUSE field of view and a velocity window of ± 1000 km s^{-1} is consistent with the field luminosity function at $z \sim 3$ (Grove et al. 2009; Cassata et al. 2011) according to which ~ 0.4 emitters should be expected above our sensitivity limit.[3] Thus, the lack of galaxies at the redshift of this metal-poor gas cloud implies that this $z \sim 3.2$ LLS arises either from a pocket of the IGM (possibly connecting faint galaxies) or from the CGM of a galaxy below our sensitivity limit. Although it is difficult to precisely estimate the physical densities and sizes of LLSs (Fumagalli et al. 2016), we note that the IGM origin is also supported by the low density and Mpc-scale size of the absorbing

---

[3] While different determinations of the luminosity function agree at $z \sim 3$, differences up to a factor of 2 in our estimates can arise when choosing different parameters from the literature. However, this uncertainty does not affect our conclusions.
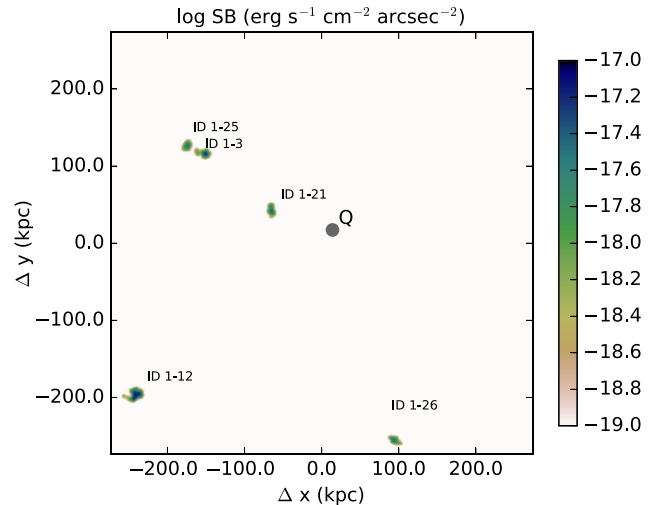
Figure 5. Spatial distribution of the Lyα emitters at the redshift of the $z \sim 3.1$ LLS. North is up, east to the left. The quasar position is marked by the grey circle. The alignment in projection of at least three Lyα emitters and a pristine LLS is suggestive of a cosmic web filament crossing the field of view in the north-east/south-west direction.

cloud (see Table 1 and Lehner et al. 2016). It should be also noted that while dust is expected to play a negligible role particularly in these chemically pristine environments, we cannot exclude biases arising from extinction based only on our data.

Conversely, when searching for Lyα emitters at the redshift of the pristine ($Z < 10^{-3.8}$ Z$_\odot$) LLS at $z \sim 3.1$, we identify five emitters (Fig. 2). Of those, ID 1-21 lies at a close impact parameter from the quasar ($D_{\text{qso}} = 77.7 \pm 0.5$ kpc) at a velocity separation of $\Delta v = 795 \pm 20$ km s^{-1} with respect to the LLS redshift. While this velocity shift is apparently high, redshifts of ~ 300–400 km s^{-1} relative to systemic are common for Lyα due to its resonant nature, and offsets up to ~ 800 km s^{-1} have been observed (Steidel et al. 2010; Rakic et al. 2011). Thus, ID 1-21 is likely to be the closest galaxy in physical space to the pristine LLS. In velocity space, instead, ID 1-12 is the closest to the LLS without considering radiative transfer effects ($\Delta v = -375 \pm 20$ km s^{-1}), but at larger projected impact parameter ($D_{\text{qso}} = 312.4 \pm 0.5$ kpc). For comparison, most of the host galaxies of the $z \sim 1$ LLSs that have been reported in the literature (e.g. Lehner et al. 2013) lie at distances of $\lesssim 100$ kpc and velocities of $\lesssim 350$ km s^{-1}.

Given that the physical three-dimensional distance from each source to the LLS is unknown, it is difficult to unambiguously identify the closest host galaxy and to directly compare to the results of simulations. However, when considered altogether, the detection of five sources in a small volume centred at the LLS redshift is an extremely rare fluctuation compared to the field number density of Lyα emitters. As discussed, adopting the Cassata et al. (2011) luminosity function, we should expect to detect ~ 0.4 emitters in this volume. Thus, the detection of five emitters corresponds to a very rare event with probability of $\sim 5 \times 10^{-5}$ of occurring at random. For this reason, we conclude that the pristine LLS lies within a 'rich' environment with a biased population of Lyα emitters, among which ID 1-21 is possibly the closest association.

Moreover, as shown in Fig. 5, at least three of the detected emitters (four if including ID 1-26) appear to lie along a line which also intersects the location where the pristine LLS is detected in absorption. Given the lack of systematic correlation in the line-of-sight velocity of these emitters, and given that Lyα is a resonant

transition, we cannot propose an unambiguous interpretation for this alignment. However, this morphology is strongly suggestive of a filament that crosses the field in the north-east/south-west direction (cf. Møller & Fynbo 2001). This feature, in conjunction with the fact that this cloud has no detectable metals but lies at close separation from at least one galaxy, supports the idea that this LLS originates from a cold stream that connects and feeds one or multiple Lyα emitters with modest SFRs. As noted above, however, the assertion that this gas is infalling is only indirectly inferred from a combination of low metallicity and proximity to one or more galaxies, as we lack direct observational evidence that the gas is indeed moving towards or inside a halo. Following this argument, even if the observed alignment of sources was coincidental and solely due to projection effects, our data would nevertheless suggest a picture in which nearly pristine gas is being accreted from the IGM inside a group of emitters.

Our work adds new constraints for the scenario put forward by modern cosmological simulations, particularly within the cold accretion paradigm (e.g. Faucher-Giguère & Kereš 2011; Fumagalli et al. 2011b, 2014a; Shen et al. 2013; Faucher-Giguère et al. 2015). On the one hand, the association of a metal-poor LLS with multiple Lyα emitters offers one of the most compelling examples of chemically pristine gas that is likely accreting on to a galaxy (or a galaxy group), in line with theoretical predictions. On the other hand, our observations uncover two different environments for these metal-poor LLSs. This cautions against blind associations between individual very-metal poor LLSs and cold streams purely relying on absorption measurements. While not ruled out, this link needs more solid footing (see e.g. Ribaudo et al. 2011; Crighton et al. 2013; Fumagalli et al. 2016).

The fact that metal-poor LLSs should not simply be connected to accretion based on their metal content alone is also reinforced by considerations on the H I column density. Indeed, besides having very low metal content, both LLSs targeted by our observations also have a relatively low column density (log $N_{\rm HI}$ = 17.2–17.4), at the limit of the threshold that defines optically thick absorbers. With the exception of some partial LLSs, studies of large samples of absorbers at $z \sim 3$ hint at a decline in the metal distribution of optically thick gas at low column densities and low physical densities (e.g. Cooper et al. 2015; Fumagalli et al. 2016; Glidden et al. 2016; Lehner et al. 2016), implying that metal-poor absorption line systems around log $N_{\rm HI} \sim 17$ may arise not only from CGM gas, but also from the IGM. Such a contribution from both CGM and IGM in low-column density and metal-poor LLSs would explain the different environments seen around these two LLSs, a conclusion which is also reinforced by the different densities and sizes inferred for these two absorbers (Table 1).

In summary, while we cannot draw far-reaching conclusions on the nature of LLSs and their connection to the CGM of galaxies from a single field, our observations place these two very metal-poor LLSs in an environment that resembles the IGM or the CGM of galaxies with very modest SFRs in one case, and in an environment that is consistent with a cold stream feeding one or more galaxies in the second case. While our results should not be trivially extrapolated to the full LLS population because very metal poor systems represent only ≲20 per cent of the LLS population at these redshifts (Fumagalli et al. 2016; Lehner et al. 2016), our analysis provides a clear indication that the claimed connection between metal-poor LLSs and star-forming galaxies fed by cold streams is plausible, but still requires empirical scrutiny across a wide range of metallicity and column density. The answer to this open question is likely within reach in the era of large-field IFUs at 8-m telescopes, thanks to dedicated observations [such as our own MUSE programme 197.A-0384(A)] that will soon target $z \sim$ 3.5 quasar fields hosting $z \sim 3$ LLSs. Combined with new observations at lower redshift, these IFU surveys will also enable detailed comparisons with studies at $z \sim 1$ that currently place most of the optically thick absorbers within ∼100 kpc of galaxies regardless to their metallicity (e.g. Lehner et al. 2013).

REFERENCES

Adelman-McCarthy J. K. et al., 2007, ApJS, 172, 634
Alam S. et al., 2015, ApJS, 219, 12
Arrigoni Battaia F., Hennawi J. F., Cantalupo S., Prochaska J. X., 2016, preprint (arXiv:1604.02942)
Asplund M., Grevesse N., Sauval A. J., Scott P., 2009, ARA&A, 47, 481
Astropy Collaboration: Robitaille T. P. et al., 2013, A&A, 558, A33
Bacon R. et al., 2010, Proc. SPIE, 7735, 9
Bertin E., Arnouts S., 1996, A&AS, 117, 393
Bielby R. et al., 2013, MNRAS, 430, 425
Birnboim Y., Dekel A., 2003, MNRAS, 345, 349
Borisova E. et al., 2016, preprint (arXiv:1605.01422)
Bouché N., Murphy M. T., Kacprzak G. G., Péroux C., Contini T., Martin C. L., Dessauges-Zavadsky M., 2013, Science, 341, 50
Brammer G. B., van Dokkum P. G., Coppi P., 2008, ApJ, 686, 1503
Cantalupo S., Lilly S. J., Haehnelt M. G., 2012, MNRAS, 425, 1992
Cantalupo S., Arrigoni-Battaia F., Prochaska J. X., Hennawi J. F., Madau P., 2014, Nature, 506, 63
Cassata P. et al., 2011, A&A, 525, A143
Cooper T. J., Simcoe R. A., Cooksey K. L., O'Meara J. M., Torrey P., 2015, ApJ, 812, 58
Crighton N. H. M., Hennawi J. F., Prochaska J. X., 2013, ApJ, 776, L18
Crighton N. H. M., Hennawi J. F., Simcoe R. A., Cooksey K. L., Murphy M. T., Fumagalli M., Prochaska J. X., Shanks T., 2015, MNRAS, 446, 18
Dekel A., Birnboim Y., 2006, MNRAS, 368, 2
Dekel A. et al., 2009, Nature, 457, 451

Faucher-Giguère C.-A., Kereš D., 2011, MNRAS, 412, L118

Faucher-Giguère C.-A., Kereš D., Ma C.-P., 2011, MNRAS, 417, 2982

Faucher-Giguère C.-A., Hopkins P. F., Kereš D., Muratov A. L., Quataert E., Murray N., 2015, MNRAS, 449, 987

Fumagalli M., O'Meara J. M., Prochaska J. X., 2011a, Science, 334, 1245

Fumagalli M., Prochaska J. X., Kasen D., Dekel A., Ceverino D., Primack J. R., 2011b, MNRAS, 418, 1796

Fumagalli M., Hennawi J. F., Prochaska J. X., Kasen D., Dekel A., Ceverino D., Primack J., 2014a, ApJ, 780, 74

Fumagalli M., O'Meara J. M., Prochaska J. X., Kanekar N., Wolfe A. M., 2014b, MNRAS, 444, 1282

Fumagalli M., O'Meara J. M., Prochaska J. X., 2016, MNRAS, 455, 4100

Fynbo J. U., Thomsen B., Møller P., 2000, A&A, 353, 457

Genzel R. et al., 2010, MNRAS, 407, 2091

Glidden A., Cooper T. J., Cooksey K. L., Simcoe R. A., O'Meara J. M., 2016, preprint (arXiv:1604.02144)

Goerdt T., Dekel A., Sternberg A., Gnat O., Ceverino D., 2012, MNRAS, 424, 2292

Grove L. F., Fynbo J. P. U., Ledoux C., Limousin M., Møller P., Nilsson K. K., Thomsen B., 2009, A&A, 497, 689

Hennawi J. F., Prochaska J. X., Cantalupo S., Arrigoni-Battaia F., 2015, Science, 348, 779

Hewett P. C., Wild V., 2010, MNRAS, 405, 2302

Kereš D., Katz N., Weinberg D. H., Davé R., 2005, MNRAS, 363, 2

Kereš D., Katz N., Fardal M., Davé R., Weinberg D. H., 2009, MNRAS, 395, 160

Kron R. G., 1980, ApJS, 43, 305

Lehner N. et al., 2013, ApJ, 770, 138

Lehner N. et al., 2016, ApJ, in press

Martin C. L., Shapley A. E., Coil A. L., Kornei K. A., Bundy K., Weiner B. J., Noeske K. G., Schiminovich D., 2012, ApJ, 760, 127

Martin D. C., Matuszewski M., Morrissey P., Neill J. D., Moore A., Cantalupo S., Prochaska J. X., Chang D., 2015, Nature, 524, 192

Møller P., Fynbo J. U., 2001, A&A, 372, L57

Oke J. B. et al., 1995, PASP, 107, 375

Planck Collaboration XVI et al., 2014, A&A, 571, A16

Prochaska J. X., Hennawi J. F., Simcoe R. A., 2013, ApJ, 762, L19

Rakic O., Schaye J., Steidel C. C., Rudie G. C., 2011, MNRAS, 414, 3265

Rauch M. et al., 2008, ApJ, 681, 856

Ribaudo J., Lehner N., Howk J. C., Werk J. K., Tripp T. M., Prochaska J. X., Meiring J. D., Tumlinson J., 2011, ApJ, 743, 207

Rubin K. H. R., Prochaska J. X., Koo D. C., Phillips A. C., 2012, ApJ, 747, LL26

Rudie G. C. et al., 2012, ApJ, 750, 67

Sancisi R., Fraternali F., Oosterloo T., van der Hulst T., 2008, A&AR, 15, 189

Schlafly E. F., Finkbeiner D. P., 2011, ApJ, 737, 103

Shen S., Madau P., Guedes J., Mayer L., Prochaska J. X., Wadsley J., 2013, ApJ, 765, 89

Steidel C. C., Erb D. K., Shapley A. E., Pettini M., Reddy N., Bogosavljevic M., Rudie G. C., Rakic O., 2010, ApJ, 717, 289

van de Voort F., Schaye J., Altay G., Theuns T., 2012, MNRAS, 421, 2809

Weilbacher P. M., Streicher O., Urrutia T., Pécontal-Rousset A., Jarno A., Bacon R., 2014, ASP Conf. Ser. Vol. 485. Astronomical Data Analysis Software and Systems XXIII. Astron. Soc. pac., San Francisco, p. 451

This paper has been typeset from a TEX/LATEX file prepared by the author.